Accepted Manuscript

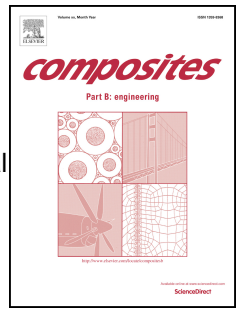

Investigation of wave propagation in piezoelectric helical waveguides with the spectral finite element method

Yingjing Liang, Yiyi Li, Yijie Liu, Qiang Han, Dianzi Liu

PII: S1359-8368(18)32674-X

DOI: 10.1016/j.compositesb.2018.09.083

Reference: JCOMB 6053

To appear in: *Composites Part B*

Received Date: 19 August 2018

Revised Date: 15 September 2018

Accepted Date: 24 September 2018

Please cite this article as: Liang Y, Li Y, Liu Y, Han Q, Liu D, Investigation of wave propagation in piezoelectric helical waveguides with the spectral finite element method, *Composites Part B* (2018), doi: https://doi.org/10.1016/j.compositesb.2018.09.083.

Investigation of wave propagation in piezoelectric helical waveguides with the Spectral Finite Element Method

Yingjing Liang[a], Yiyi Li[a], Yijie Liu[a,*], Qiang Han[b], Dianzi Liu[c]

[a]*Department of Engineering Mechanics,School of Civil Engineering, Guangzhou University, Guangzhou 510640, China*
[b]*Department of Engineering Mechanics, School of Civil Engineering and Transportation, South China University of Technology, Guangzhou, PR China*
[c]*Faculty of Science, University of East Anglia, Norwich, UK*

Abstract

The dispersion behaviors of wave propagation in waveguides of piezoelectric helical structures are investigated. By using the tensor analysis in the helical curve coordinate, the general strain−displacement relationship of piezoelectric helix is firstly considered. This paper's formulation is based on the spectral finite element which just requires the discretization of the cross-section with high-order spectral elements. The eigenvalue matrix of the dispersion relationship between wavenumbers and frequencies is obtained. Numerical examples on PZT5A and $Ba_2NaNb_5O_{15}$ helical waveguides of a wide range of lay angles are presented. The effects of the piezoelectric on the dispersive properties and the variation tendency of dispersion curves on helix angles are shown. The mechanism of mode separation in piezoelectric helical waveguides is further analyzed through studying waves structures of the flexural modes.

Keywords: Dispersion behavior Piezoelectric helical structures High-order spectral elements Spectral finite element

1. Introduction

Piezoelectric devices with helical structures are widely used as sensors and actuators in a variety of mechanical, civil and aerospace applications at

*Corresponding author
Email address: liuyijie1987@outlook.com (Dianzi Liu)

various scales, such as helical piezoelectric springs[1], net shape formed spiral actuators[2],helical-shaped piezoelectric motors[3], helical piezoelectric fiber actuators[4] and magnetic helical micro-machines[5]. All these applications require the accurate knowledge of the dispersive properties for designing and optimizing piezoelectric devices, seeing that new opportunities are opened for the control of the electric field using dynamic elastic waves.

Currently, the system of theories of common piezoelectric structures has achieved a satisfactory level. Tiersten[6] developed the linear piezoelectric equations of the infinite thick anisotropic plate and discussed the dispersive characteristics of wave propagation. Paul et al.[7] derived the dispersion relation of axial motion of a hollow circular cylinder of piezoelectric ceramics by using Fourier transform method. The cut-off frequencies on electric and elastic wave propagation of piezoelectric composite plate can be found in Stewart et al.[8]. Wang[9] investigated the wave propagation in a piezoelectric coupled cylindrical shell structure based on a membrane shell model. The characteristic surfaces of waves in a hybrid multilayered piezoelectric circular cylinder was considered by Han et al.[10] through an analytical-numerical method.

Maradudin et al.[11] firstly presented the orthogonal function method to study wave propagation in homogeneous semi-infinite wedges. This method had the material coefficient relation instead of the stress-free and electric boundary condition by using the pulse function and then simplified the dynamic differential equation into the quadratic eigenproblem. Yu[12] proposed Legendre polynomials method to investigate the waveguide behavior in continuous functionally graded plates. The wave propagation in multilayered hollow cylinders was analyzed by Yu[13] through an extension of an improvement of the Legendre polynomial approach. However, the orthogonal function method is only applicable to simple cross section and develops the dissymmetric eigenmatrix to the disadvantage of the solution of the dispersion curves. In this paper, the spectral finite element(SFE) is presented to analyze the dispersion properties of elastic waves in piezoelectric helical waveguides. If geometrical and material parameters of waveguides are invariant along the wave propagation direction, SFE as an efficient tool can extract the dispersion relationship. As an improvement of the finite element method(FEM), SFE can reduce a three-dimensional problem of waveguides to a two-dimensional one. So only the cross section is needed to mesh through this approach. In addition, the higher-order spectral elements(Gauss-Lobatto-Legendre) can increase the computational efficiency compared the traditional linear and

quadratic elements. Because the integration points coincide with the element nodes, many entries of the coefficient and mass matrices become zero. The mass matrix becomes diagonal and the stiffness matrix is diagonal in the case of isotropic material behavior and block-diagonal otherwise, particularly to the benefit of the computation of matrix inversion. The final solution of the dispersion equation derived by SFM becomes an eigenvalue problem of a Hamiltonian matrix.

SFE algorithms was originally proposed by Lysmer[14](1970) to analyze the behavior of Rayleigh waves in semi-infinite multilayered elastic waveguides. Subsequently, The work of Treyssede[15] had demonstrated that the structures possessing the property of translational invariance along its axis, such as composite cylinders[16], fluid filled cylinders[17], functionally graded cylinders[18], straight bars of arbitrary cross section[19], helical rods[20] can be considered to investigate the dispersion behavior of elastic wave by using the SFE formulation.. As for applications of piezoelectric waveguides, Taciroglu et al.[21] presented SFE to study wave propagation of laminated piezoelectric cylinders. Cortes [22] presented the dispersion relation of phase and group velocities in a periodic array of multi-layered piezoelectric plates with finite and arbitrary cross sections and presented useful information for the design and optimization of such transducers.

The present paper is organized as follows: in Section 2, the helical coordinate system is proposed based on Frenet-Serrets principle and the helical coordinate with a set of orthogonal unit basis (introduced as the contravariant basis) is considered, where components of tensor retain the dimension of original quantity.

The general strain−displacement relationship of piezoelectric helix including the relationship of electric field strength and electric potential is then obtained via the tensor analysis method in Section 3.

In section 4, the formulation of the SFM of piezoelectric helical waveguides is presented based on the Fourier transform and the variational principle.

In section 5, the combination between modified modal assurance criterion (M-MAC) and the Pade expansion is used to sort modes, which takes advantage of the convenient programming of M-MAC and the fast and reliable alternative of the Pade expansion. Mode differentiation is helpful for the study of the trends of influence factors on wave propagation.

Finally, some dispersion curves of helical structures of a wide range of lay angles on PZT5A and $Ba_2NaNb_5O_{15}$ are given in section 6. The piezoelectric

effect on wave propagation of piezoelectric helical waveguides is analyzed and the change rule on the waveguide behavior is obtained by compared with the dispersion relations of phase and group velocities of different lay angles. Furthermore, the properties of cut-off frequency and mode transition for elastic wave propagation is discussed in details and the wave structures of the flexural modes is calculated to explain the mechanism of mode separation.

2. Helical coordinate system

As shown in Fig.1, the helix centerline with the arclength parameter s can be described in the Cartesian orthonormal $(\mathbf{e}_x, \mathbf{e}_y, \mathbf{e}_z)$ as

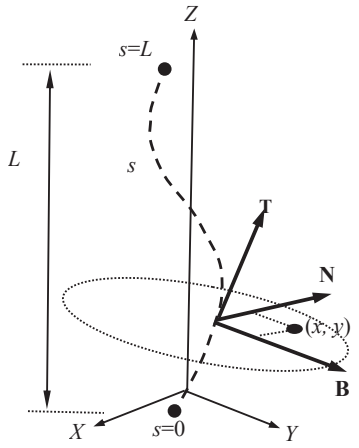

Fig. 1. Helix coordinate system based on the Frenet-Serret formula

$$\mathbf{R}(s) = R_0 \cos\left(\frac{2\pi}{l}s\right)\mathbf{e}_x + R_0 \sin\left(\frac{2\pi}{l}s\right)\mathbf{e}_y + \frac{L}{l}s\mathbf{e}_z \tag{1}$$

where l is the length of one turn of the helix centerline, R_0 and L are the radius of the helix and the pitch along Z axis, respectively. The unit tangent, normal, and binormal vectors to the helix centerline, expressed by $\mathbf{T}$, $\mathbf{N}$ and $\mathbf{B}$ (see Fig.1), or collectively the Frenet-Serret frame, are obtained from $\mathbf{T}(s) = d\mathbf{R}/ds$ and the Frenet-Serret principle: $d\mathbf{T}/ds = -\kappa\mathbf{N}, d\mathbf{N}/ds = \tau\mathbf{B}+\kappa\mathbf{T}, d\mathbf{B}/ds = -\tau\mathbf{N}$, which together form an orthonormal basis spanning the three-dimensional Euclidean space. Note that $\mathbf{N}$ is oriented outward the

curvature. For the helix, the curvature κ and the tortuosity τ are constants, which can be expressed as $4\pi^2 R_0^2/l^2$ and $2\pi L/l$, respectively.

A local coordinate system$(x-y)$ can be built on the $(\mathbf{N}-\mathbf{B})$ plate. Any point in a helical coordinate can be written from the orthonormal basis $(\mathbf{N},\mathbf{B},\mathbf{T})$ as a position vector Φ:

$$\mathbf{\Phi}(x,y,s)=\mathbf{R}(s)+x\mathbf{N}(s)+y\mathbf{B}(s) \tag{2}$$

In the sequel, the notation (x,y,s) is denoted as (x_1,x_2,x_3) for simplicity. Utilizing the Frenet-Serret formula, we obtain the non-orthogonal natural basis from the expression $\mathbf{g}_i=\partial\mathbf{\Phi}/\partial x_i\,(i=1,2,3)$:

$$\begin{aligned}\mathbf{g}_1&=\mathbf{N}(s)\\ \mathbf{g}_2&=\mathbf{B}(s)\\ \mathbf{g}_3&=-\tau y\mathbf{N}(s)+\tau x\mathbf{B}(s)+(1+\kappa y)\mathbf{T}(s)\end{aligned} \tag{3}$$

Then, the covariant metric tensor yields $G_{ij}=\mathbf{g}_i\mathbf{g}_j$, given in matrix form by

$$G=\begin{bmatrix}1 & 0 & -\tau y\\ 1 & 0 & \tau x\\ -\tau y & \tau x & \tau^2(x^2+y^2)+(1+\kappa x)^2\end{bmatrix} \tag{4}$$

If the governing equation is directly deduced based on the natural basis by using the tensor analysis method, the physical components of the tensor must be consistent with the original dimension of physical quantities in mathematical physics. Since the non-orthogonal natural basis considered in this paper is not holonomic, which may not have the property of retaining the original dimension. We need to introduce a set of orthogonal unit vectors $\mathbf{g}_i$ as the covariant basis. Here, the Frenet-Serret frame is chosen as

$$\mathbf{g}_{(1)}=\mathbf{N}(s),\quad \mathbf{g}_{(2)}=\mathbf{B}(s),\quad \mathbf{g}_{(3)}=\mathbf{T}(s) \tag{5}$$

The transformation between the above two bases is given by

$$\mathbf{g}_{(i)}=\beta_{ij}\mathbf{g}_j\quad\text{or}\quad \mathbf{g}_i=\beta'_{ij}\mathbf{g}_{(j)}\quad(i,j=1,2,3) \tag{6}$$

where β and $\beta^{'}$ are given by

$$\beta = \frac{1}{1+\kappa x}\begin{bmatrix} 1+\kappa x & 0 & \tau y \\ 0 & 1+\kappa x & -\tau x \\ 0 & 0 & 1 \end{bmatrix} \tag{7}$$

$$\beta^{'} = \begin{bmatrix} 1 & 0 & 0 \\ 0 & 1 & 0 \\ -\tau y & \tau x & 1+\kappa x \end{bmatrix} \tag{8}$$

The contravariant basis $\mathbf{g}^i$ of the helical coordinate defined by $\mathbf{g}_i\mathbf{g}^i = \delta_i^j$ is given by

$$\begin{aligned} \mathbf{g}^1 &= \mathbf{N}(s) + \frac{\tau y}{(1-\kappa x)}\mathbf{T}(s) \\ \mathbf{g}^2 &= \mathbf{B}(s) - \frac{\tau x}{(1+\kappa x)}\mathbf{T}(s) \\ \mathbf{g}^3 &= \frac{1}{(1+\kappa x)}\mathbf{T}(s) \end{aligned} \tag{9}$$

3. General strain-displacement relation of piezoelectric helix

In the helical coordinate, the displacement field is decried in a way of the metric tensor as

$$\mathbf{U}{=}u_i\mathbf{g}_{(i)}{=}u_1\mathbf{g}_{(1)} + u_2\mathbf{g}_{(2)} + u_3\mathbf{g}_{(3)} \tag{10}$$

where u_i is the components of the displacement tensor. As the elastic wave propagation is considered in this paper, Small strain is needed only to consider, whose strain-displacement relation is linear. The strain tensor can be defined by the second order tensor as

$$\begin{aligned} \boldsymbol{\varepsilon} &= \varepsilon_{ij}\mathbf{g}_{(i)}\mathbf{g}_{(j)} = 1/2\left(\nabla\mathbf{U} + \mathbf{U}\nabla\right) \\ &= \frac{1}{2}\left(\mathbf{g}^i\frac{\partial\mathbf{U}}{\partial x_i} + \frac{\partial\mathbf{U}}{\partial x_i}\mathbf{g}^i\right) \end{aligned} \tag{11}$$

where ∇ represents the gradient operator of the metric tensor.

For most of piezoelectric devices, their sizes are much smaller than wavelengths with respect to work frequencies, therefore the electric-magnetic field associating with the stress field is regarded as an electrostatic field. The function of the electric-field intensity can be described as a gradient of the electric

potential as follow

$$\mathbf{E} = E_i \mathbf{g}_{(i)} = -\nabla\phi = -\frac{\partial\phi}{\partial x_i}\mathbf{g}^i \tag{12}$$

where $\mathbf{E}$ and ϕ are the electric-field intensity and electric potential, respectively.

Rewriting above two equations, the general strain is obtained as

$$\begin{aligned}\bar{\boldsymbol{\varepsilon}} = [&\varepsilon_{11}\mathbf{g}_{(1)}\mathbf{g}_{(1)}, \varepsilon_{22}\mathbf{g}_{(2)}\mathbf{g}_{(2)}, \varepsilon_{33}\mathbf{g}_{(3)}\mathbf{g}_{(3)},\\ &2\varepsilon_{12}\mathbf{g}_{(1)}\mathbf{g}_{(2)}, 2\varepsilon_{13}\mathbf{g}_{(1)}\mathbf{g}_{(3)}, 2\varepsilon_{23}\mathbf{g}_{(2)}\mathbf{g}_{(3)},\\ &-E_1\mathbf{g}_{(1)}, -E_2\mathbf{g}_{(2)}, -E_3\mathbf{g}_{(3)}]^T\\ &= \mathbf{b}_1\bar{\mathbf{u}}_{,x} + \mathbf{b}_2\bar{\mathbf{u}}_{,y} + \mathbf{b}_s\bar{\mathbf{u}}_{,s} + \mathbf{b}_0\bar{\mathbf{u}}\end{aligned} \tag{13}$$

where the general displacement tensor is given by $\bar{\mathbf{u}} = \begin{bmatrix} u_1 & u_2 & u_3 & -\phi \end{bmatrix}^T$, and the differential operation matrices $\mathbf{b}_0, \mathbf{b}_1, \mathbf{b}_2, \mathbf{b}_s$ are shown in Appendix A.

4. Numerical method

When studying the dispersive behavior of the piezoelectric helical waveguides, the length of the structure is considered to be infinite. As the curvature and tortuosity of the helix are constants, the curvature degree does not vary along its axis. Besides that, the shape and material parameters are invariant with respect to s. Due to these two reasons, the piezoelectric helical structure has the property of translational invariance, in which waves can generally travel without reflection.

The constitutive relationship of the linear stress−strain −electrical field in matrix form is given by

$$\begin{aligned}\bar{\boldsymbol{\sigma}} = [&\sigma_{11}\mathbf{g}_{(1)}\mathbf{g}_{(1)}, \sigma_{22}\mathbf{g}_{(2)}\mathbf{g}_{(2)}, \sigma_{33}\mathbf{g}_{(3)}\mathbf{g}_{(3)},\\ &\sigma_{12}\mathbf{g}_{(1)}\mathbf{g}_{(2)}, \sigma_{13}\mathbf{g}_{(1)}\mathbf{g}_{(3)}, \sigma_{23}\mathbf{g}_{(2)}\mathbf{g}_{(3)},\\ &D_1\mathbf{g}_{(1)}, D_2\mathbf{g}_{(2)}, D_3\mathbf{g}_{(3)}]^T = \mathbf{H}^*\bar{\varepsilon}\end{aligned} \tag{14}$$

where $\bar{\boldsymbol{\sigma}}$ is a metric tensor of the general stress containing the stress components and the electric displacements, and $\mathbf{H}^*$ is the constitutive matrix containing the elastic constants $\mathbf{C}$, dielectric constants $\mathbf{v}$ and the piezoelec-

tric constants $\mathbf{e}$[23]

$$\mathbf{H}^* = \begin{bmatrix} \mathbf{C} & -\mathbf{e}^T \\ \mathbf{e} & \mathbf{v} \end{bmatrix} \tag{15}$$

The vibrational formulation of electrodynamics based on the Hamilton principle can be obtained as

$$\delta \int_t \int_V \left(\frac{1}{2} \bar{\boldsymbol{\varepsilon}}^T \mathbf{H} \bar{\boldsymbol{\varepsilon}} + \frac{1}{2} \dot{\bar{\mathbf{u}}}^T \boldsymbol{\rho} \dot{\bar{\mathbf{u}}} \right) dV dt - \delta \int_t \int_\Gamma \bar{\mathbf{u}} \bar{\mathbf{f}} d\Gamma dt = 0 \tag{16}$$

with

$$\mathbf{H} = \begin{bmatrix} \mathbf{C} & -\mathbf{e}^T \\ -\mathbf{e} & -\mathbf{v} \end{bmatrix} \quad \boldsymbol{\rho} = \begin{bmatrix} \rho & & & \\ & \rho & & \\ & & \rho & \\ & & & 0 \end{bmatrix} \tag{17}$$

The load vector $\bar{\mathbf{f}}$ on the cross section Γ is described as

$$\bar{\mathbf{f}}(r, \theta, z, t) = [t_{zz} \;\; t_{zx} \;\; t_{zy} \;\; D_r]^T \tag{18}$$

The cross section of the waveguides is discretized by using high-order spectral elements. In the following steps, we show the derivations of SFM formulation by using the isoparametric element. In an element of order p, there are $p+1$ nodes. The position of nodes $\xi_i, \eta_j \subseteq [-1, 1]$, i, j in $1, 2, \cdots, (p+1)$ are obtained as roots of the following polynomial:

$$\begin{array}{c} (1-\xi^2) P'_p(\xi) = 0 \\ (1-\eta^2) P'_p(\eta) = 0 \end{array} \tag{19}$$

and weights obey:

$$w_{i,j} = \frac{2}{p(p+1)(P_p(\xi_i))^2} \times \frac{2}{p(p+1)(P_p(\eta_j))^2} \tag{20}$$

where P'_p denotes the first derivative of Legendre polynomial degree p. The Lagrangian interpolation is expressed as

$$N_{i,j}(\xi, \eta) = \prod_{k=1, j \neq i}^{p+1} \frac{\xi - \xi_i}{\xi_k - \xi_i} \prod_{l=1, j \neq j}^{p+1} \frac{\xi - \xi_j}{\xi_l - \xi_j} \tag{21}$$

And The transformation between the local coordinate (ξ, η) and the global coordinate (x, y) is given via the mapping function $N_i(\xi, \eta)$ as

$$\begin{aligned} x(\xi, \eta) &= N_M(\xi, \eta) x_M \\ y(\xi, \eta) &= N_M(\xi, \eta) y_M \end{aligned} \tag{22}$$

where x_M and y_M are global coordinates of the corresponding nodes. M in $N_M(\xi, \eta)$ equals to $(j-1) \times p + i$.

To transform the differential operator of Eq.22 to the local coordinate, the coordinate relation is required:

$$\begin{bmatrix} \partial_\xi \\ \partial_\eta \end{bmatrix} = \mathbf{J} \begin{bmatrix} \partial_x \\ \partial_y \end{bmatrix}, \partial_s = \partial_s \tag{23}$$

with the Jacobian matrix

$$\mathbf{J} = \begin{bmatrix} x_{,\xi} & x_{,\xi} \\ y_{,\eta} & y_{,\eta} \end{bmatrix} \tag{24}$$

The general displacement amplitudes of one element on the cross section in terms of the local coordinate are interpolated by shape functions. Hence, with the nodal general displacements $\bar{\mathbf{U}}$ such displacements is approximated by

$$\bar{\mathbf{u}}(\xi, \eta, s) = \mathbf{N}(\xi, \eta) \bar{\mathbf{U}}(s) \tag{25}$$

where $\mathbf{N}$ denotes the matrix of shape function. Substituting Eq.25 into Eq.12, the general strain is obtained as

$$\bar{\boldsymbol{\varepsilon}} = \mathbf{B}_1 \bar{\mathbf{U}}(s) + \mathbf{B}_s \bar{\mathbf{U}}(s)_{,s} \tag{26}$$

where

$$\mathbf{B}_s = \mathbf{b}_s \mathbf{N} \tag{27}$$

$$\begin{aligned} \mathbf{B}_1 = \frac{1}{|\mathbf{J}|}(y_{,\eta}\mathbf{b}_1 - x_{,\eta}\mathbf{b}_2)\mathbf{N}_{,\xi} \\ + \frac{1}{|\mathbf{J}|}(-y_{,\xi}b_1 + x_{,\xi}b_2)\mathbf{N}_{,\eta} + b_0\mathbf{N} \end{aligned} \tag{28}$$

Substituting Eq.18, Eq.25 and Eq.26 into Eq.16, after the integration by parts, we can obtain

$$\int_t \int_s \bigcup_{e=1}^{n_{el}} \delta(\bar{\mathbf{U}}^e)^T \left[\mathbf{E}_3^e \bar{\mathbf{U}}^e, ss + \left(\mathbf{E}_2^e - (\mathbf{E}_2^e)^T\right) \bar{\mathbf{U}}^e, s - \mathbf{E}_1 \bar{\mathbf{U}}^e - \mathbf{M}^e \bar{\mathbf{U}}^e_{,tt} + \mathbf{F}^e\right] dsdt = \mathbf{0} \tag{29}$$

where n_{el} is a number of high order spectral elements; The superscript e of $\bar{\mathbf{U}}$ presents the sequence number, of element; $\mathbf{E}_1^e, \mathbf{E}_2^e, \mathbf{E}_3^e, \mathbf{M}^e$ and $\mathbf{F}^e$ are expressed in Appendix A

Base on the approach of the finite element method, we assemble the above element mass and stiffness matrices into global matrices in the standard manner to yield a discrete system of dispersion equation. Besides, the weak form of Eq.28 is replaced by the below equation in the integral symbol.

$$\left[\mathbf{E}_3 \bar{\mathbf{U}}, ss + \left(\mathbf{E}_2 - (\mathbf{E}_2)^T\right) \bar{\mathbf{U}}, s - \mathbf{E}_1 \bar{\mathbf{U}} - \mathbf{M} \bar{\mathbf{U}}_{,tt} + \mathbf{F}\right] = \mathbf{0} \tag{30}$$

After application of the two-dimension Fourier transform in terms of the time and axial evolution, Eq.30 can be changed to the equation in the frequency-wavenumber domain for the consider disperser point $(\omega.k)$

$$\left[\mathbf{E}_1 + ik\left(\mathbf{E}_2 - \mathbf{E}_2^T\right) - k^2 \mathbf{E}_3 + \omega^2 \mathbf{M}\right] \widetilde{\mathbf{U}} = \widetilde{\mathbf{F}} \tag{31}$$

where the $\widetilde{\mathbf{F}}$ and $\widetilde{\mathbf{U}}$ can be expressed as

$$\begin{aligned} \widetilde{\mathbf{F}}_{(k,\omega)} &= \int_{-\infty}^{+\infty} \int_{-\infty}^{+\infty} \mathbf{F}(s,t) e^{-i(\omega t - ks)} d\omega dt \\ \widetilde{\mathbf{U}}_{(k,\omega)} &= \int_{-\infty}^{+\infty} \int_{-\infty}^{+\infty} \bar{\mathbf{U}}(s,t) e^{-i(\omega t - ks)} d\omega dt \end{aligned} \tag{32}$$

where $\widetilde{\mathbf{U}}$ denotes the amplitude of the general displacement with respect to the $k - \omega$ domain.

The high-order spectral element is employed. Owing to the superposition between the integration points and the nodes and the Kronecher delta of the interpolation basis function, the above stiffness and mass matrixes can all be simplified into diagonal sparse matrixes to reduce the memory space consumption and improve the computational efficiency. So the above general eigenvalue problem can be predigested into a linear standard problem.

$$(\boldsymbol{\lambda}\mathbf{I} - \mathbf{A})\boldsymbol{\varphi} = \mathbf{B} \tag{33}$$

with

$$\mathbf{A} = \begin{bmatrix} \mathbf{E}_3^{-1}\mathbf{E}_2^T & -\mathbf{E}_3^{-1} \\ \omega^2\mathbf{M} - \mathbf{E}_1 + \mathbf{E}_2\mathbf{E}_3^{-1}\mathbf{E}_2^T & -\mathbf{E}_2\mathbf{E}_3^{-1} \end{bmatrix} \quad \mathbf{B} = \begin{bmatrix} \mathbf{0} \\ \widetilde{\mathbf{F}} \end{bmatrix} \tag{34a}$$

$$\boldsymbol{\varphi} = [\widetilde{\mathbf{U}}, \widetilde{\mathbf{Q}}]^T \quad \lambda = ik \tag{34b}$$

where $\mathbf{I}$ is unit matrix, whose size is the same as $\mathbf{A}$; λ and $\boldsymbol{\varphi}$ are the eigenvalue and eigenvector of the matrix $\mathbf{A}$, and $\widetilde{\mathbf{Q}}$ denotes the nodal force matrix

$$\widetilde{\mathbf{Q}} = (\lambda\mathbf{E}_3 + \mathbf{E}_2)\,\widetilde{\mathbf{U}} \tag{35}$$

Non-trivial solutions of Eq.34 are obtained by imposing that the determinant of the coefficient's matrix of $\boldsymbol{\varphi}$ must vanish:

$$det\,[\boldsymbol{\lambda}\mathbf{I} - \mathbf{A}] = 0 \tag{36}$$

If there are n nodes in the cross section, A is a $8n \times 8n$ matrix. At a given frequency ω, the wave numbers λ can be calculated by using the Choleshy decomposition of the *eig* functions in MATLAB software. $\mathbf{J}$ is defined by

$$\mathbf{J} = \begin{bmatrix} \mathbf{0} & \mathbf{I}_{4n} \\ -\mathbf{I}_{4n} & \mathbf{0} \end{bmatrix} \tag{37}$$

where $\mathbf{I}_{4n}$ is a $4n \times 4n$ unitary matrix. We can find that

$$(\mathbf{JA})^T = (\mathbf{JA}) \tag{38}$$

Here shows that A is a Hamiltonian matrix. So, if λ is an eigenvalue of Eq.33, $-\lambda$, then λ^* and $-\lambda^*$ are also eigenvalues, where the subsript $*$ denotes the complex conjugate. The $\pm$ of wave numbers respresent postive-going and negative-going wave types, respectively. All eigenvalues are classified into two categories:

$$\begin{cases} \lambda_i, & \text{if } \Re(\lambda_i) < 0 \text{ or } \Re(\lambda_i) > 0 \text{ and } \wp(\lambda_i) > 0 \\ \lambda_{m+i}, & \text{if } \lambda_i + \lambda_{m+i} = 0, \quad i \in [1, 2, 3 \cdots m] \end{cases} \tag{39}$$

where $\Re$ and $\wp$ demotes the real and imaginary part of eigenvalues, respectively.

Associated with each eigenvalue λ_i and λ_i are the $\boldsymbol{\varphi}_i$ and $\boldsymbol{\varphi}_j$ complex eigenvectors representing the modal displacement amplitudes, also known as wave structures. The complex eigenvectors satisfy the following symplectic orthogonality relation:

$$\begin{cases} \boldsymbol{\varphi}_i^T \mathbf{J} \boldsymbol{\varphi}_j = 0, \quad \boldsymbol{\varphi}_j^T \mathbf{J} \boldsymbol{\varphi}_i = 0, \quad \text{when} \quad \lambda_i + \lambda_j \neq 0 \\ \boldsymbol{\varphi}_i^T \mathbf{J} \boldsymbol{\varphi}_{m+i} = d_i, \quad \boldsymbol{\varphi}_{m+i}^T \mathbf{J} \boldsymbol{\varphi}_i = -d_i, \quad \text{when} \quad \lambda_i + \lambda_{m+i} = 0 \end{cases} \tag{40}$$

In the same time, they also satisfy this condition:

$$\begin{cases} \boldsymbol{\varphi}_i^T \mathbf{J} \mathbf{A} \boldsymbol{\varphi}_j = 0, \quad \text{when} \quad \lambda_i + \lambda_j \neq 0 \\ \boldsymbol{\varphi}_i^T \mathbf{J} \mathbf{A} \boldsymbol{\varphi}_{m+i} = d_i \lambda_i, \quad \text{when} \quad \lambda_i + \lambda_{m+i} = 0 \end{cases} \tag{41}$$

where d_i is a complex coefficient.

Given ω and suppressing excitation, the solution $\widetilde{\mathbf{U}}$ of Eq.33, which is the forced response under the excitation $\widetilde{\mathbf{F}}$, is now expanded as a sum of guided modes:

$$\widetilde{\mathbf{U}} = \sum_{j=1}^{8n} \alpha_j \widetilde{\mathbf{U}}_j \tag{42}$$

where $8n$ is the numbers of modes, but truncated in practice.

Substituting the eigenmode expansion into Eq.33 and Pre-multiplying this equation with $\mathbf{J}$, we can obtain

$$\boldsymbol{\varphi}_{m+j}^T \sum_{k=1}^{8n} \left[\mathbf{J}\mathbf{A} - \lambda \mathbf{J} \right] \alpha_k \boldsymbol{\varphi}_k = \boldsymbol{\varphi}_{m+j}^T \mathbf{J} \mathbf{B} \tag{43}$$

Taking advantage of symplectic orthogonality relation, α_j are calculated:

$$\alpha_j = \frac{\boldsymbol{\varphi}_{m+j}^T \mathbf{J} \mathbf{B}}{d_j \left(\lambda - \lambda_j \right)} \tag{44}$$

The displacement response in the wavenumber-frequency domain is

$$\widetilde{\mathbf{U}}(\omega, k) = \sum_{j=1}^{8n} \frac{\boldsymbol{\varphi}_{m+j}^T \mathbf{J} \mathbf{B}}{d_j \left(\lambda - \lambda_j \right)} \widetilde{\mathbf{U}}_j(\omega, k) \tag{45}$$

We evaluate the displacement in the space-frequency domain by using the

inverse Fourier transform as

$$\bar{\mathbf{U}}(\omega, s) = \frac{1}{2\pi} \sum_{j=1}^{8n} \int_{-\infty}^{+\infty} \frac{\boldsymbol{\varphi}_{m+j}^T \mathbf{J}\mathbf{B}}{d_j \left(\lambda - \lambda_j\right)} \widetilde{\mathbf{U}}_j(\omega, k) e^{iks} dk \tag{46}$$

Assuming that $\mathbf{B}$ is holomorphic, based on the Cauchy's residue theorem, the displacement yields to

$$\bar{\mathbf{U}}(\omega, s) = \sum_{j=1}^{8n} \frac{\boldsymbol{\varphi}_{m+j}^T \mathbf{J}\mathbf{B}}{i d_j} \widetilde{\mathbf{U}}_j(\omega, k) e^{\lambda_j s} \tag{47}$$

The phase velocity v_p is given by ω/k, and the group velocity c_g can be defined as

$$c_g = \frac{\partial \omega}{\partial k} = i \frac{\partial \omega}{\partial \lambda} \tag{48}$$

Group velocities are obtained as utilizing the above gradient algorithm, which requires to group the results that represent the same mode by using modal differentiation. Besides that, the accuracy relates to the given step of the frequency ω. This paper directly calculates group velocities via the operation of above eigenmatrices. $\boldsymbol{\varphi}_L = (\widetilde{\mathbf{U}}_L, \widetilde{\mathbf{Q}}_L)$ and $\boldsymbol{\varphi}_R = (\widetilde{\mathbf{U}}_R, \widetilde{\mathbf{Q}}_R)$ associated with each eigenvalue λ are defined as the right and left-hand side eigenvectors of Eq.36. They yield to, respectively

$$-\mathbf{A}^T \boldsymbol{\varphi}_L = \lambda \boldsymbol{\varphi}_L, \quad -\mathbf{A}\boldsymbol{\varphi}_R = \lambda \boldsymbol{\varphi}_R \tag{49}$$

By taking the derivative of Eq.31, we obtain

$$\left((\mathbf{E}_2 - \mathbf{E}_2^T) + 2\lambda \mathbf{E}_3 - 2i\omega c_g \mathbf{M}\right) \widetilde{\mathbf{U}}_R = 0 \tag{50}$$

Pre-multiplying this above equation with $\widetilde{\mathbf{U}}_L^T$ and simultaneously post-multiplying with $\widetilde{\mathbf{U}}_R$, we obtain

$$\widetilde{\mathbf{U}}_L^T \left((\mathbf{E}_2 - \mathbf{E}_2^T) + 2\lambda \mathbf{E}_3 - 2i\omega c_g \mathbf{M}\right) \widetilde{\mathbf{U}}_R = 0 \tag{51}$$

The displacement vector and nodal force vector should satisfy

$$\widetilde{\mathbf{Q}}_R = \left(\lambda \mathbf{E}_3 + \mathbf{E}_2\right) \widetilde{\mathbf{U}}_R \quad \widetilde{\mathbf{Q}}_L = \left(-\lambda \mathbf{E}_3 + \mathbf{E}_2\right) \widetilde{\mathbf{U}}_L \tag{52}$$

Substituting Eq.52 into Eq.51, the group velocity is given by

$$c_g = i\frac{\widetilde{\mathbf{U}}_L^T\widetilde{\mathbf{Q}}_R - \widetilde{\mathbf{Q}}_L^T\widetilde{\mathbf{U}}_R}{2\omega\widetilde{\mathbf{U}}_L^T\mathbf{M}\widetilde{\mathbf{U}}_R} \tag{53}$$

5. Mode sorting

The scatter plot of dispersion behavior is calculated from Eq.33. It is difficult to sort those dispersion curves in the form of modal differentiation, which groups those information that belongs to the same mode. However, modal differentiation is conducive to interpret properties of different modes. It is also necessary to analyze some further problem, such as wave scattering, time-transient response and source influence. Via the symplectic property of Eq.40 instead of the similarity of the normalized eigenvetors belonging to the same mode[24], modified modal assurance criterion (M-MAC) establishes the principle about solution points of the two-adjacent frequencies:

$$\mathrm{mac}_{ij}^{NM} = \left(\left(\boldsymbol{\varphi}_i^N\right)^T\mathbf{J}\boldsymbol{\varphi}_{M+j}^M\right) \tag{54}$$

where N and M are indices of mode group, and i and j are two adjacent points of one frequency step. The minimum value mac_{ij}^{NM} represents that the eigenvector $\boldsymbol{\varphi}_i^N$ and $\boldsymbol{\varphi}_j^M$ belong to the same mode. However, in a frequency range of mode transition where wave structure changes very fast, M-MAC does not guarantee that $\boldsymbol{\varphi}_i^N$ and $\boldsymbol{\varphi}_j^M$ belong to the same mode. Moreover, this convergence result highly depends on the frequency step.

The Padé expansion is employed by [24], which takes advantage of the differentiation of the group velocities. Compared with the Taylor polynomial, the Padé expansion has faster convergence rate. The Padé expansion of order [1/2] is given by

$$\tilde{k}_i^N = \frac{\gamma_i^0 + \alpha_i^1\Delta\omega}{1 + \beta_i^1\Delta\omega + \beta_i^2\Delta\omega^2} \tag{55}$$

where the above coefficients can be defined in Appendix A and $\Delta\omega$ is the frequency increment. By using the Pade expansion approach, $\tilde{k}_i^N$ is obtained as an approximate wavenumber of the post-wavenumber of the N^{th} mode. For each mode, $\tilde{k}_i^N$ is compared with each real solution of the next wavenumber.

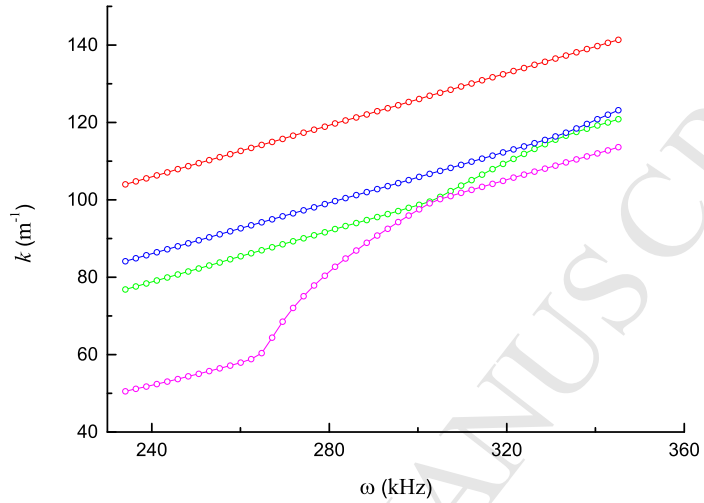

(a) Frequency spectrum

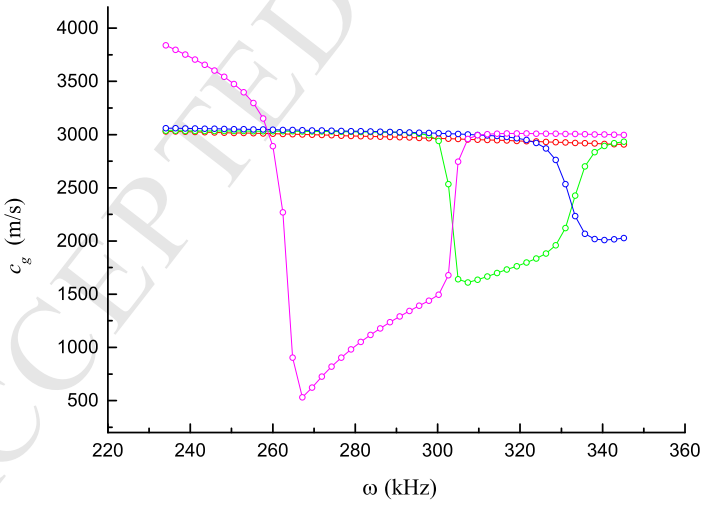

(b) Group velocity curves

Fig. 2. Modal differentiation of some selected modes (Scatter − initial solution, Solid line− solution of modal differentiation)

The deviation is given by

$$\Delta_{ij}^{NM} = \left| \frac{\tilde{k}_i^N - k_j^M}{k_j^M} \right| \tag{56}$$

The minimum value Δ_{ij}^{NM} indicates the pre-wavenumber k_i^N and the post-wavenumber k_j^M belonging to the same mode. However, to compute the coefficients of Eq.A-3, the three wavenumbers k_0^N, k_1^N, k_2^N are needed, which brings large difficulty into the program of modal differentiation. This paper adopts the coupling method of MAC and the Padé expansion. M-MAC is used to track mode in the global frequencies but the Padé expansion is employed to check modal differentiation in a frequency range of mode transition. As shown in Fig.2, this proposed method obtains the desirable accuracy by comparing scatter plot and curves of mode differentiation.

6. Numerical Results

Without loss of generality, we can choose variables adimensionalised with some parameters, length a and time ω/c_s. Thus, the dimensionless frequency and wavenumber are given by $\Omega = \omega a/c_s$ and $K = ka$ respectively, where a and c_s are the radius of the cross section and the shear wave velocity $\sqrt{C_{44}/\rho}$, respectively. In this section, we consider the dispersion relations of PZT5A and $Ba_2NaNb_5O_{15}$ helical structures with the cross section radius $2.5mm$, helix radius $5mm$ and various lay angles. The physical properties of the PZT5A and $Ba_2NaNb_5O_{15}$ material are listed in Table.1. c_s is computed as the material properties of PZT5A.

Table 1
Material properties on PZT5A and $Ba_2NaNb_5O_{15}$

Property	c_{11}	c_{12}	c_{13}	c_{22}	c_{23}	c_{33}	c_{44}	c_{55}	c_{66}
$Ba_2NaNb_5O_{15}$	24.7	5.2	10.4	13.5	5	23.9	6.5	7.6	6.6
PZT5A	12	7.51	7.51	11.1	7.51	12	2.1	2.1	2.1
Property	v_{11}	v_{22}	v_{33}	e_{14}	e_{36}	e_{21}	e_{22}	e_{23}	ρ
$Ba_2NaNb_5O_{15}$	201	28	196	3.4	2.8	-0.3	4.3	-0.4	5.3
PZT5A	916	830	916	8.4	8.4	-2.8	16.4	-2.8	7.75

Units $c_{ij}(10N/m^2)$,$v_{ij}(10^{-11}), e_{ij}(C/m), \rho(kg/m^3)$[12]

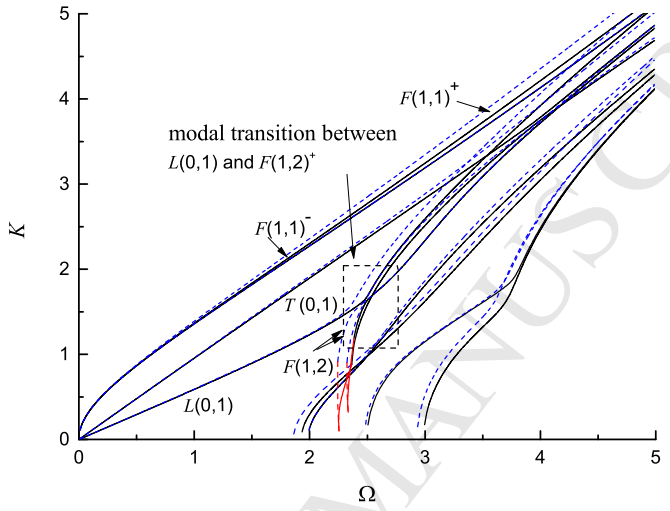

(a) Frequency spectrum on $Ba_2NaNb_5O_{15}$

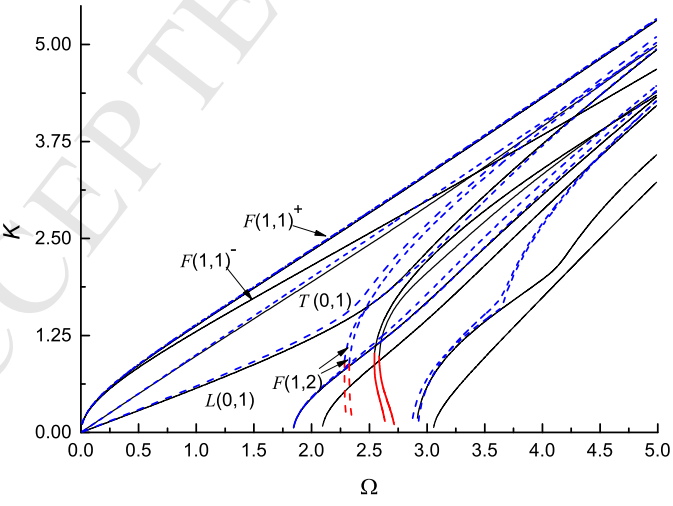

(b) Frequency spectrum on PZT5A

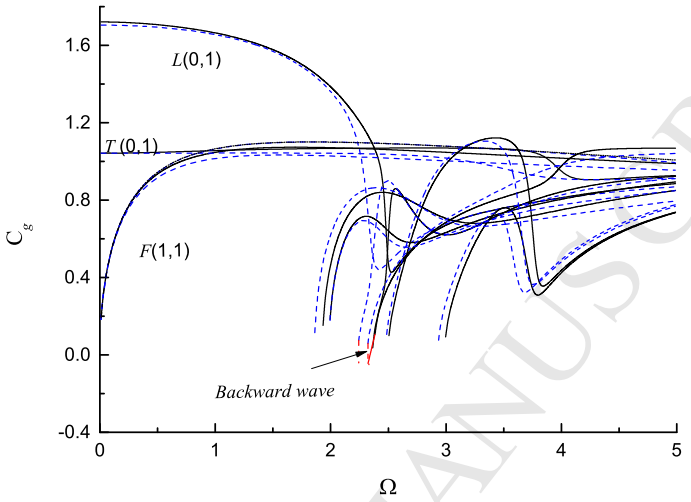

(c) Group velocity curves on $Ba_2NaNb_5O_{15}$

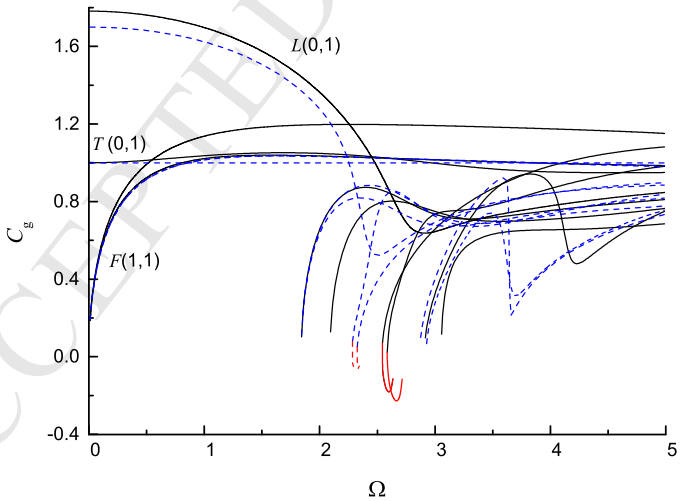

(d) Group velocity curves on PZT5A

Fig. 3. Frequency spectrum and energy velocity curves of a circular bar for ranging from 0 and 5. Left: $Ba_2NaNb_5O_{15}$. Right: PZT5A. Scatter – non-piezoelectric, solid line – piezoelectric

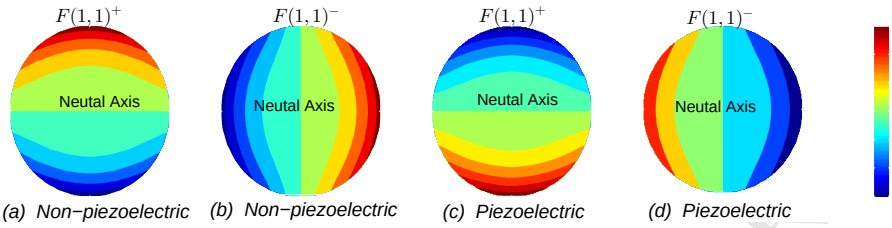

Fig. 4. Wave structures of the flexural on the $Ba_2NaNb_5O_{15}$ material for $\Omega = 2$

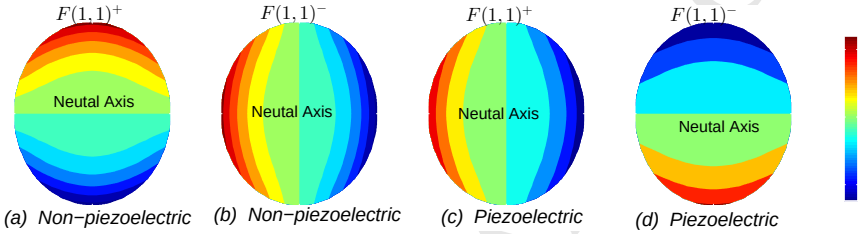

Fig. 5. Wave structures of the flexural on the PZT5A material for $\Omega = 2$

We can observe from Fig.3(a) that the flexural mode $F(1,1)$ of non-piezoelectric has two curves, which are denoted as $F(1,1)^-$ and $F(1,1)^+$, respectively. The phenomenon called mode separation may result from the difference of elastic constants between the x and y direction. However, it is difficult to check mode separation of the flexural modes of non-piezoelectric in Fig.3(b). Compared with the frequency spectrum curves of non-piezoelectric, the phenomenon of mode separation of the flexural mode $F(1,1)$ on the two materials after considering the piezoelectric effect becomes even more obvious. The piezoelectric effect on the overall trend of the longitudinal $L(0,1)$ is not apparent, the whole group velocity curve of piezoelectric just moves a little bit to the right compared with the curve of non-piezoelectric. In an intermediate frequency range, the group velocities of the longitudinal $L(0,1)$ of piezoelectric are faster than those of the non-piezoelectric. Similar to the steel helical waveguides, it is easy to observe that the modal transition between $L(0,1)$ and $F(1,2)^+$ occurs around the notch frequencies, as shown in the rectangle box of Fig.3(a). Compared with the flexural $F(1,1)$ and longitudinal $F(1,1)$, the torsional $T(0,1)$ is less influenced by the piezoelectric property.

As for axisymmetric waveguides bars , the wave structures of the $F(1,1)^+$ mode are the same as that of the $F(1,1)^-$ mode. Phase velocities and wavenumbers of the two modes are identical for any frequencies, thus the

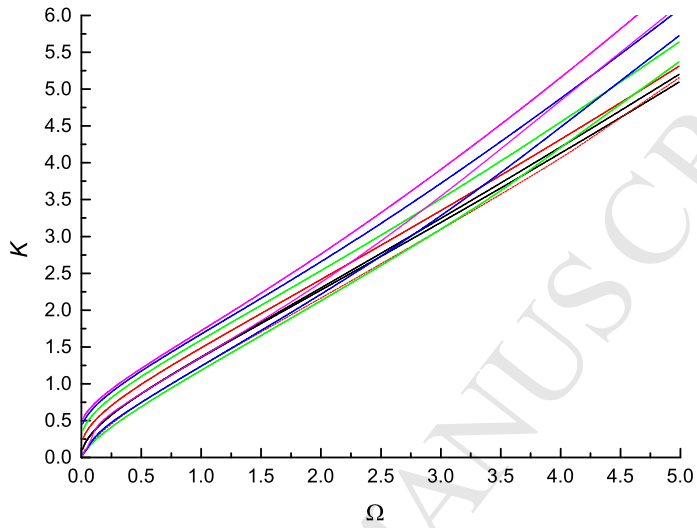

(a) Frequency spectrum of $F(1,1)$ on $Ba_2NaNb_5O_{15}$

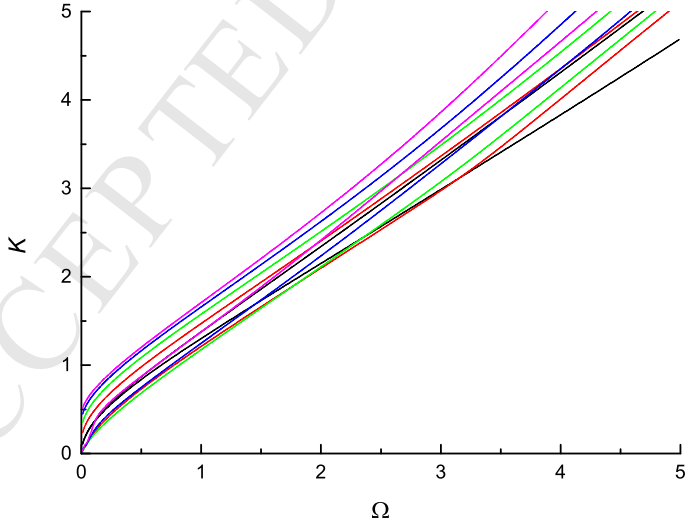

(b) Frequency spectrum of $F(1,1)$ on PZT5A

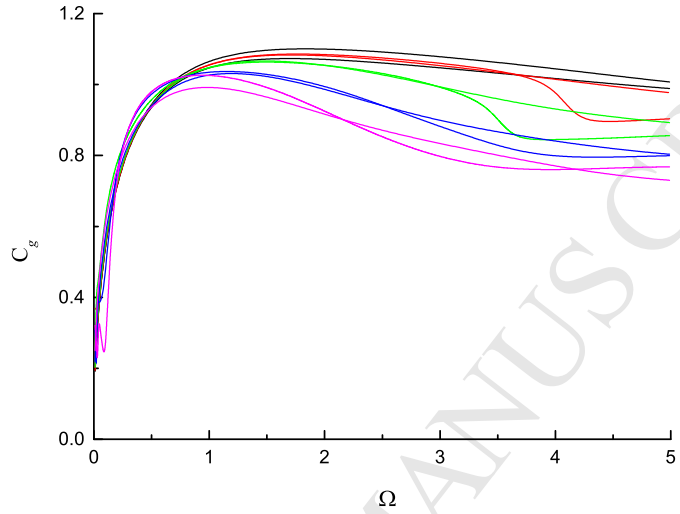

(c) Group velocity curves of $F(1,1)$ on $Ba_2NaNb_5O_{15}$

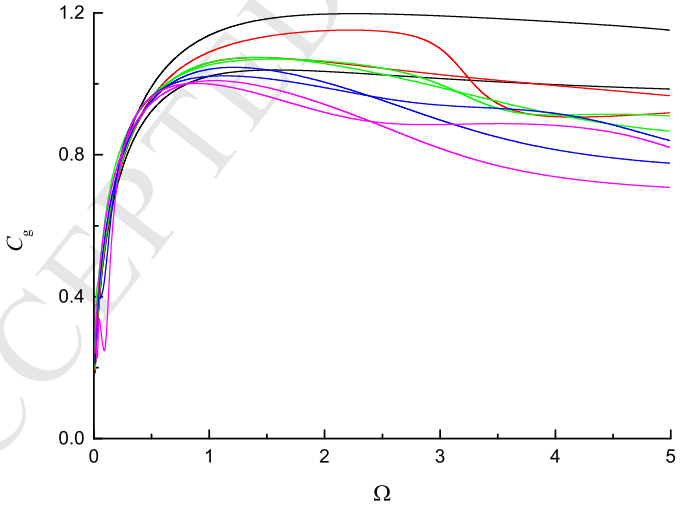

(d) Group velocity curves of $F(1,1)$ on PZT5A

Fig. 6. Frequency spectrum and energy velocity curves of the flexural $F(1,1)$ mode for ranging from 0 and 5. Left: $Ba_2NaNb_5O_{15}$. Right: PZT5A. Black-0^0 , Red-15^0 , Green-30^0 Blue-45^0 , Magenta-60^0

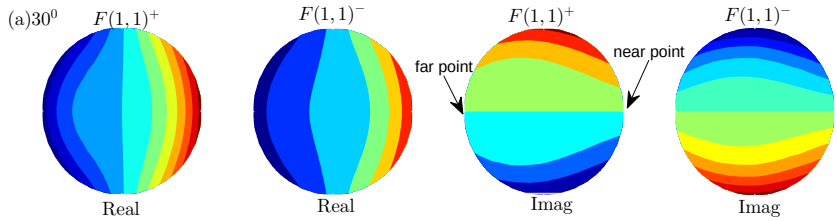

(a) Lay angle 30^0 on the $Ba_2NaNb_5O_{15}$ material

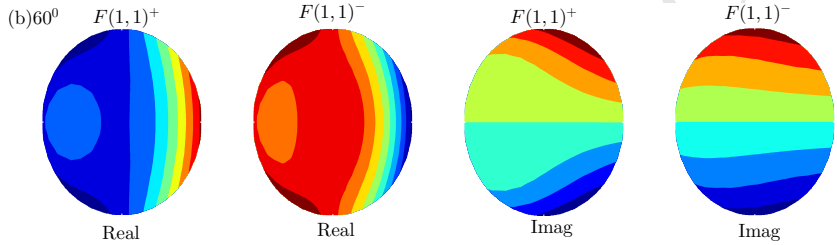

(b) Lay angle 60^0 on the $Ba_2NaNb_5O_{15}$ material

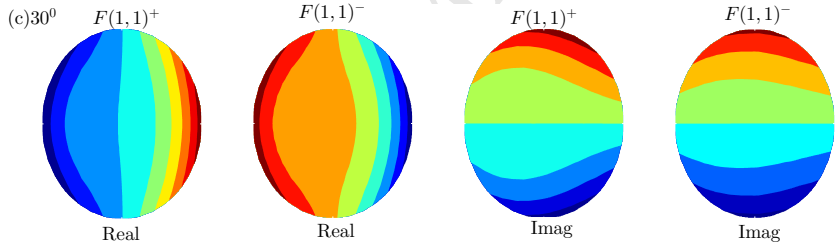

(c) Lay angle 30^0 on the PZT5A material

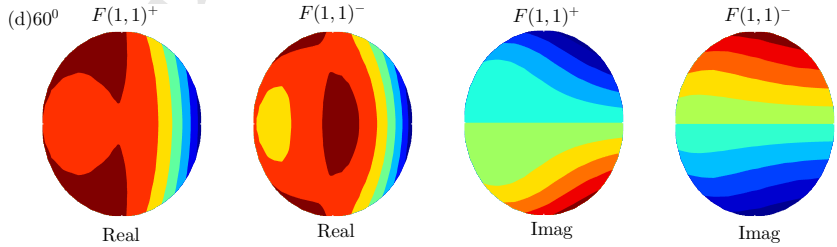

(d) Lay angle 60^0 on the PZT5A material

Fig. 7. Wave structures of the flexural $F(1,1)$ of piezoelectric helical waveguides on the PZT5A and $Ba_2NaNb_5O_{15}$ material for $\Omega = 2$

two frequency spectrum curves overlap each other perfectly. So the phenomenon of mode separation does not occur. The dynamic basis of the 1st

order flexural along the axis s is only one and the vibration space of the 1th order flexural is one-dimensional. In other words, the displacement along any central axis are all the same.

Fig.4 and Fig.5 give wave structures of the flexural $F(1,1)$ on PZT5A and $Ba_2NaNb_5O_{15}$, respectively. Real components of above wave structures is comparatively infinitesimal with imaginary components and can be ignored. It is easy to check that the central axes of wave structures of cross sections of the $F(1,1)^-$ and $F(1,1)^+$ modes are two symmetric axes for the material parameters (the x and y directions). The relationship between the clouds plots of two modes is not symmetry perfectly and the vibration forms along wave propagation is different and the wavenumber of one mode for a given frequency along the axis s does not equal to the other mode. So the dispersion curves of the $F(1,1)^-$ and $F(1,1)^+$ modes do not overlap perfectly in the phenomenon called as mode separation. By contrast of the wave structures on PZT5A and $Ba_2NaNb_5O_{15}$, it is discovered that the phenomenon of mode separation becomes much more obvious with increasing the difference of the material parameters between the x and y directions. The vibration space of the 1th order flexural is two-dimensional. The displacement deformations along any central axis should consist of the $F(1,1)^-$ and $F(1,1)^+$ modes.

The frequency spectrum and group velocity curves of the flexural $F(1,1)$ mode of piezoelectric helical waveguides are shown in Fig.6. The helical geometry has a large impact on wave propagation, which means that the piezoelectric helical rod cannot be simplified into the piezoelectric bar. In a low-intermediate frequency range, the wavenumber gap between the two modes increases as the lay angle increases. In other words, the phenomenon of mode separation becomes much more obvious with the lay angle increasing. In the meantime, energy velocities of the corresponding modes decrease as the lay angle increases. If the length of one turn of the centerline becomes longer with the increment of the lay angle, the time of wave propagation along the z direction is shortened. As the frequency tends to infinity, the limit value of the 1st order flexural mode decreases with the increase of the lay angle.

In Fig.7, we show the wave structures of the flexural $F(1,1)$ mode of piezoelectric helical waveguides corresponding to 30^0, 60^0. Due to the impact of the helical geometry, the eigenmatrix $\mathbf{A}$ becomes asymmetric so that the real components of eigenvectors do not equal zero . We find that the imagine wave structures change sharply around near points which inside the cross section is nearest from the Z axis but the gradient variation becomes smaller

around far points. Moreover, there is only one symmetry axis along the x direction. Compared with the cloud maps of the imagine displacements, the real wave structures become very complex. Their central axes are not straight lines but curves. So the two central axes of the 1st flexural mode after vectors superposition of the imagine and real clouds maps are not orthogonal. Changes of wave structures become much more obvious as the lay angle increases and convex-concave shapes arise in the real clouds map.

Fig.8 and Fig.9 present the group velocity vs. frequency curves of the longitudinal $L(0,1)$ and torsional $T(0,1)$ respectively, for a wide range of lay angles. In a frequency range , the group velocities of above two modes decrease as the lay angle increases.In a high frequency range, their dispersive behaviors are very distinct, which exhibits the increasing helix effect on wave propagation with an increasing lay angle. As shown in Fig.9(a), it is easy to check mode transition between $L(0,1)$ and $F(1,2)$ in energy velocity curves of all lay angles on the $Ba_2NaNb_5O_{15}$ material. These previous curves run backwards in order to avoid a collision between $L(0,1)$ and $F(1,2)$ in the neighborhood of $\Omega = 2.4$, thanks to the piezoelectric effect. The phenomenon of mode transition between $L(0,1)$ and $F(1,2)$ doesn't appear in the dispersive behavior of 0^0 and 60^0 helical waveguide on the PZT5A material.

As shown in Fig.10, back-ward waves occur in the frequency spectrum curves of $F(1,1)^+$ of all lay angles on the two materials in a low frequency range. The frequency range of back-ward wave becomes larger with an increasing lay angle, while the phase velocities of the flexural modes get smaller. Compared with piezoelectric bars, both the longitudinal $L(0,1)$ and the torsional $T(0,1)$ of the piezoelectric helical waveguides have cut-off frequencies. Moreover, as the lay angle increases, cut-off frequency of corresponding mode increases. For a given lay angle, the cut-off frequency on the PZT5A material is larger than that of the corresponding mode on the $Ba_2NaNb_5O_{15}$ material, which further proves that the dispersive behavior becomes much more obvious as the average ratio of piezoelectric parameters to elastic constants increases or the average ratio of piezoelectric parameters to elastic constants decreases.

7. Conclusions

This paper presents the utilization of the SFM to study wave propagation of piezoelectric helical waveguides. The helical coordinate system is chosen to describe the geometry of the helical structure. The Frenet-Serrets frame

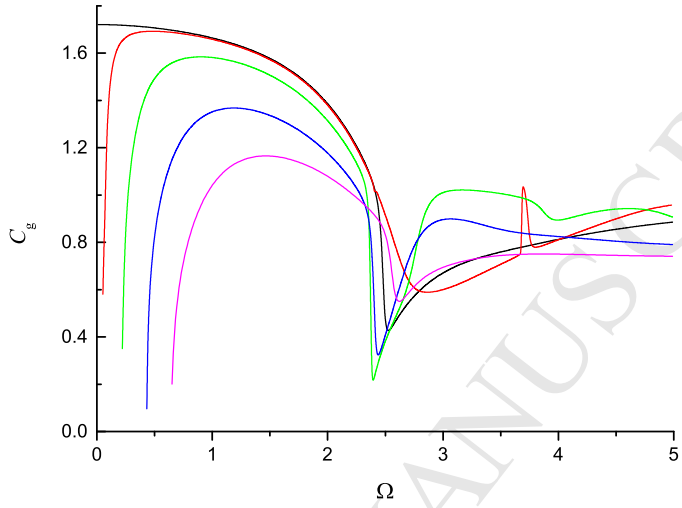

(a) Frequency spectrum of $L(0,1)$ on $Ba_2NaNb_5O_{15}$

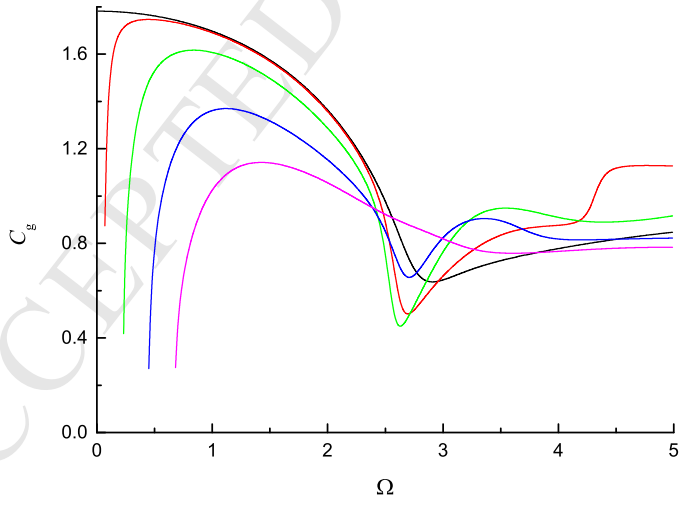

(b) Frequency spectrum of $L(0,1)$ on PZT5A

Fig. 8. Frequency spectrum and energy velocity curves of the flexural $L(0,1)$ mode for ranging from 0 and 5. Black-0^0 , Red-15^0 , Green-30^0 Blue-45^0 , Magenta-60^0

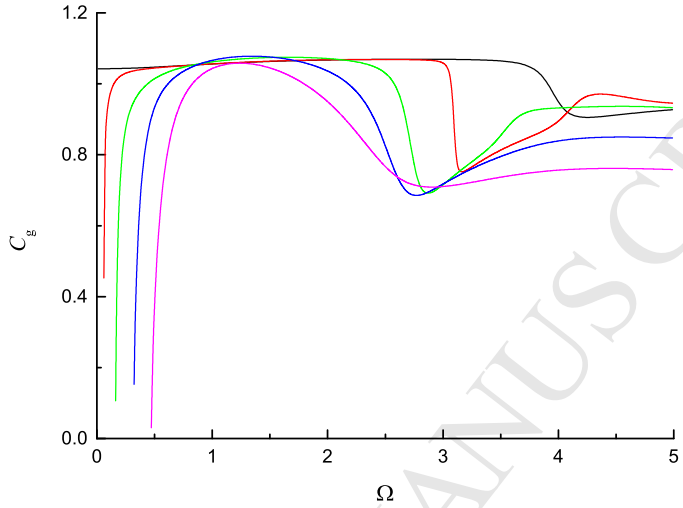

(a) Frequency spectrum of $T(0,1)$ on $Ba_2NaNb_5O_{15}$

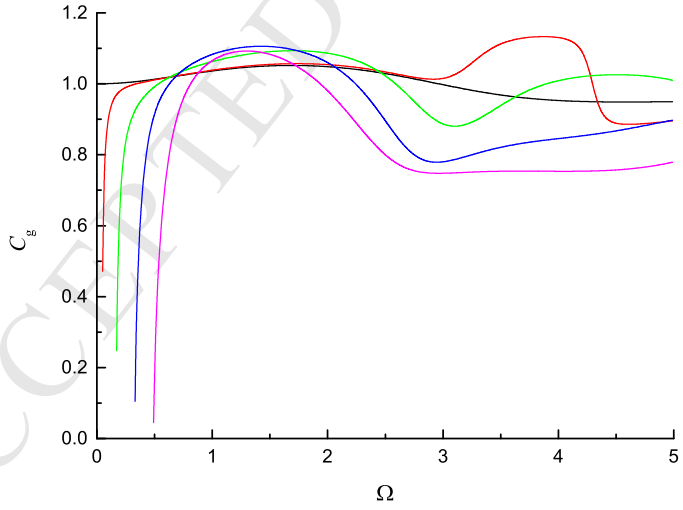

(b) Frequency spectrum of $T(0,1)$ on PZT5A

Fig. 9. Frequency spectrum and energy velocity curves of the flexural $T(0,1)$ mode for ranging from 0 and 5. Black-0^0 , Red-15^0 , Green-30^0 Blue-45^0 , Magenta-60^0

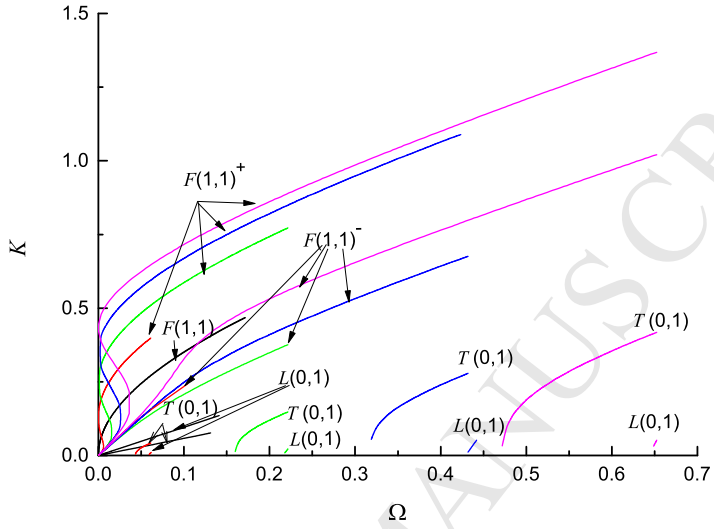

(a) Frequency spectrum on $Ba_2NaNb_5O_{15}$

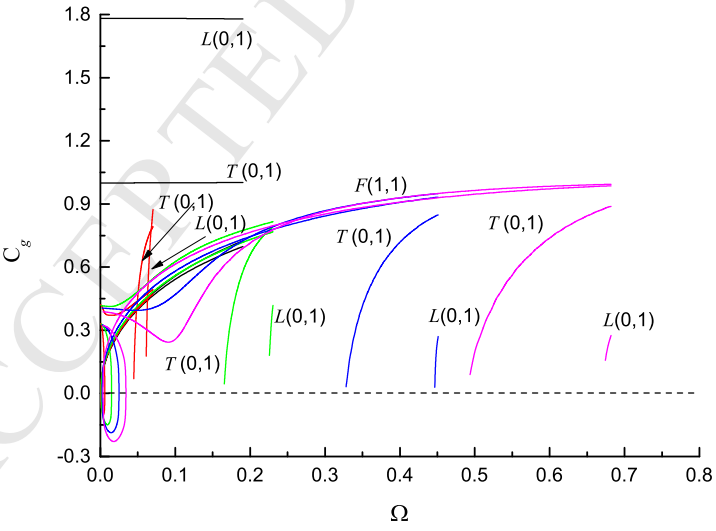

(b) Frequency spectrum on PZT5A

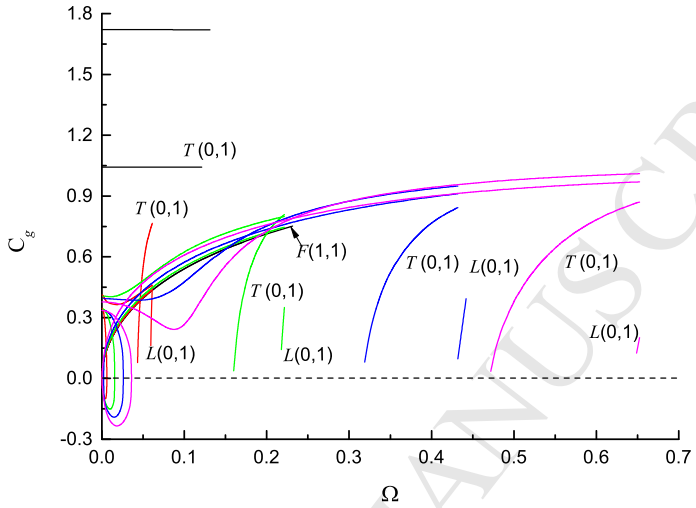

(c) Group velocity curves on $Ba_2NaNb_5O_{15}$

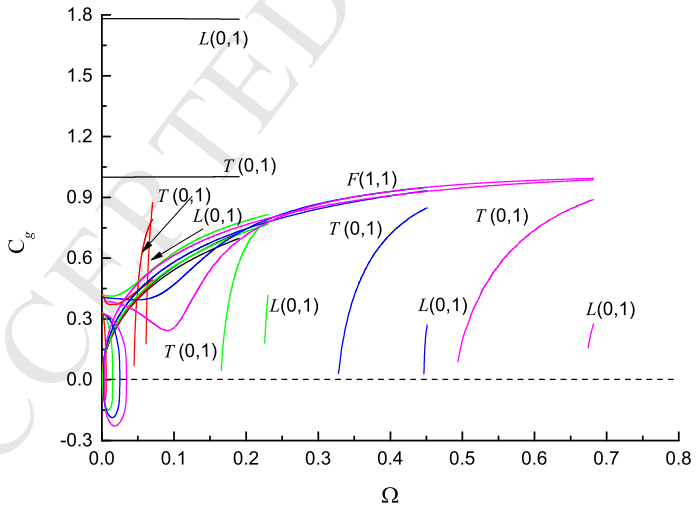

(d) Group velocity curves on PZT5A

Fig. 10. Frequency spectrum and energy velocity curves of piezoelectric helical waveguides in a low frequency range. Left: $Ba_2NaNb_5O_{15}$. Right: PZT5A. Black-0^0 , Red-15^0 , Green-30^0 Blue-45^0 , Magenta-60^0.

is introduced as the contravariant basis, where the tensor components retain the dimension of original quantity. Then, the general strainCdisplacement relationship is established via the tensor analysis method. The dispersion equation of discretization of piezoelectric helical waveguides is obtained based on the Fourier transform and the variational principle. Finally, we present the spectrum frequency and group velocity curves of PZT5A and $Ba_2NaNb_5O_{15}$ helical structures for a wide range of lay angles. We point out that the trend of the piezoelectric effect on wave propagation of piezoelectric helical waveguides and discuss the cut-off frequency, mode transition and mode separation on elastic wave propagation in details. Furthermore, wave structures of the flexural modes are calculated to explain the mechanism of mode separation.

Acknowledgements

The authors wish to acknowledge the support from by the National Natural Science Foundation of China (Grant No. 11702067 and 11472108 and 11772130)), Guangdong Province (Grant No.2016A030313617 and No.2018A030310310), and the Foundation for Young Talents in Higher Education of Guangdong, China (Grant No. 2015KQNCX122)

APPENDIX. Equations related to Section 3-5

In Section 3, the differential operation matrices in Eq.13 are given by

$$\mathbf{b}_s = \begin{bmatrix} 0 & 0 & 0 & 0 \\ 0 & 0 & 0 & 0 \\ 0 & 0 & A & 0 \\ 0 & 0 & 0 & 0 \\ A & 0 & 0 & 0 \\ 0 & A & 0 & 0 \\ 0 & 0 & 0 & 0 \\ 0 & 0 & 0 & 0 \\ 0 & 0 & 0 & A \end{bmatrix} \tag{A-1a}$$

$$\mathbf{b}_0 = \begin{bmatrix} 0 & 0 & 0 & 0 \\ 0 & 0 & 0 & 0 \\ A\kappa & 0 & 0 & 0 \\ 0 & 0 & 0 & 0 \\ 0 & -A\tau & -A\kappa & 0 \\ A\tau & 0 & 0 & 0 \\ 0 & 0 & 0 & 0 \\ 0 & 0 & 0 & 0 \\ 0 & 0 & 0 & 0 \end{bmatrix} \tag{A-1b}$$

$$\mathbf{b}_1 = \begin{bmatrix} 1 & 0 & 0 & 0 \\ 0 & 0 & 0 & 0 \\ 0 & 0 & A\tau y & 0 \\ 0 & 1 & 0 & 0 \\ A\tau y & 0 & 1 & 0 \\ 0 & A\tau y & 0 & 0 \\ 0 & 0 & 0 & 1 \\ 0 & 0 & 0 & 0 \\ 0 & 0 & 0 & A\tau y \end{bmatrix} \tag{A-1c}$$

$$\mathbf{b}_2 = \begin{bmatrix} 0 & 0 & 0 & 0 \\ 0 & 1 & 0 & 0 \\ 0 & 0 & -A\tau x & 0 \\ 1 & 0 & 0 & 0 \\ -A\tau x & 0 & 0 & 0 \\ 0 & -A\tau x & 1 & 0 \\ 0 & 0 & 0 & 0 \\ 0 & 0 & 0 & 1 \\ 0 & 0 & 0 & -A\tau x \end{bmatrix} \tag{A-1d}$$

where $A = (1 + \kappa x)$

The stiffness and mass matrices shown in Eq.?? can be expressed as

$$\mathbf{M} = \int_{\Gamma^e} \mathbf{N}^T \bar{\boldsymbol{\rho}} \mathbf{N} \left|\mathbf{J}\right| \sqrt{g} d\xi d\eta \tag{A-2a}$$

$$\mathbf{E}_1 = \int_{\Gamma^e} \mathbf{B}_1^T \mathbf{H} \mathbf{B}_1 \left|\mathbf{J}\right| \sqrt{|g|} d\xi d\eta \tag{A-2b}$$

$$\mathbf{E}_2 = \int_{\Gamma^e} \mathbf{B}_1^T \mathbf{H} \mathbf{B}_s \left|\mathbf{J}\right| \sqrt{|g|} d\xi d\eta \tag{A-2c}$$

$$\mathbf{E}_3 = \int_{\Gamma^e} \mathbf{B}_s^T \mathbf{H} \mathbf{B}_s \left|\mathbf{J}\right| \sqrt{|g|} d\xi d\eta \tag{A-2d}$$

The coefficients of the Padé expanssion are given as

$$\gamma_i^0 = k_i^N \tag{A-3a}$$

$$\gamma_i^1 = \frac{1}{c_{gi}^N} \tag{A-3b}$$

$$\gamma_i^2 \approx \frac{1}{2\Delta\omega} \left(\frac{1}{c_{gi}^N} - \frac{1}{c_{g(i-1)}^N} \right) \tag{A-3c}$$

$$\gamma_i^3 \approx \frac{1}{6\Delta\omega^2} \left(\frac{1}{c_{gi}^N} - \frac{1}{c_{g(i-2)}^N} + \frac{1}{c_{g(i-1)}^N} \right) \tag{A-3d}$$

$$\beta_i^2 = \frac{\left(\gamma_i^2\right)^2 - \gamma_i^3 \gamma_i^1}{\left(\gamma_i^1\right)^2 - \gamma_i^2 \gamma_i^0} \tag{A-3e}$$

$$\beta_i^2 = -\frac{\gamma_i^2 + \gamma_i^0 \beta_i^2}{\gamma_i^1} \tag{A-3f}$$

$$\alpha_i^1 = \gamma_i^1 + \gamma_i^0 \beta_i^1 \tag{A-3g}$$

References

[1] B. Jiao, J. Zhang, Torsional modes in piezo helical springs., IEEE transactions on ultrasonics, ferroelectrics, and frequency control 46 (1) (1998) 147–151.

[2] D. Pearce, K. Seffen, T. Button, Net shape formed spiral and helical piezoelectric actuators, Journal of materials science 37 (15) (2002) 3117–3122.

[3] S.-M. Lee, C.-S. Park, H.-E. Kim, K.-W. Lee, Helical-shaped piezoelectric motor using thermoplastic co-extrusion process, Sensors and Actuators A: Physical 158 (2) (2010) 294–299.

[4] C. L. Pan, Z. H. Feng, Y. T. Ma, W. W. Shao, Y. B. Liu, Coupled torsional and longitudinal vibrations of piezoelectric fiber actuator with helical electrodes, Ultrasonics, Ferroelectrics and Frequency Control, IEEE Transactions on 58 (4) (2011) 829–837.

[5] K. E. Peyer, S. Tottori, F. Qiu, L. Zhang, B. J. Nelson, Magnetic helical micromachines, Chemistry-A European Journal 19 (1) (2013) 28–38.

[6] H. F. Tiersten, Thickness vibrations of piezoelectric plates, The Journal of the Acoustical Society of America 35 (1) (1963) 53–58.

[7] H. Paul, M. Venkatesan, Vibrations of a hollow circular cylinder of piezoelectric ceramics, The Journal of the Acoustical Society of America 82 (3) (1987) 952–956.

[8] J. Stewart, Y.-K. Yong, Exact analysis of the propagation of acoustic waves in multilayered anisotropic piezoelectric plates, Ultrasonics, Ferroelectrics and Frequency Control, IEEE Transactions on 41 (3) (1994) 375–390.

[9] Q. Wang, Wave propagation in a piezoelectric coupled cylindrical membrane shell, International journal of solids and structures 38 (46) (2001) 8207–8218.

[10] X. Han, G. Liu, T. Ohyoshi, Dispersion and characteristic surfaces of waves in hybrid multilayered piezoelectric circular cylinders, Computational Mechanics 33 (5) (2004) 334–344.

[11] A. Maradudin, R. Wallis, D. Mills, R. Ballard, Vibrational edge modes in finite crystals, Physical Review B 6 (4) (1972) 1106.

[12] J. Yu, J. Lefebvre, Y. Guo, Free-ultrasonic waves in multilayered piezoelectric plates: An improvement of the legendre polynomial approach for multilayered structures with very dissimilar materials, Composites Part B: Engineering 51 (2013) 260–269.

[13] J. Yu, J. Lefebvre, Guided waves in multilayered hollow cylinders: The improved legendre polynomial method, Composite Structures 95 (2013) 419–429.

[14] J. Lysmer, Lumped mass method for rayleigh waves, Bulletin of the Seismological Society of America 60 (1) (1970) 89–104.

[15] F. Treyssède, Mode propagation in curved waveguides and scattering by inhomogeneities: application to the elastodynamics of helical structures, The Journal of the Acoustical Society of America 129 (4) (2011) 1857–1868.

[16] K. H. Huang, S. B. Dong, Propagating waves and edge vibrations in anisotropic composite cylinders, Journal of Sound and Vibration 96 (3) (1984) 363C379.

[17] Z. Xi, G. Liu, K. Lam, H. Shang, A strip-element method for analyzing wave scattering by a crack in a fluid-filled composite cylindrical shell, Composites Science and Technology 60 (10) (2000) 1985C1996.

[18] X. Han, G. R. Liu, Z. C. Xi, K. Y. Lam, Characteristics of waves in a functionally graded cylinder, International Journal for Numerical Methods in Engineering 53 (3) (2002) 653C676.

[19] I. Bartoli, A. Marzani, F. L. D. Scalea, E. Viola, Modeling wave propagation in damped waveguides of arbitrary cross-section, Health Monitoring and Smart Nondestructive Evaluation of Structural and Biological Systems V 295 (3-5) (2006) 685–707.

[20] F. Treyssde, Elastic waves in helical waveguides, Wave Motion 45 (2008) 457C470.

[21] S. B. Dong, E. Taciroglu, C. K. Chun, C. W. Liu, Analysis of laminated piezoelectric circular cylinders under axisymmetric mechanical and electrical loads with a semi-analytic finite element method, International Journal of Solids and Structures 41 (2004) pgs. 5185–5208.

[22] D. H. Cortes, S. K. Datta, O. M. Mukdadi, Elastic guided wave propagation in a periodic array of multi-layered piezoelectric plates with finite cross-sections, Ultrasonics 50 (3) (2010) 347–356.

[23] D. H. Cortes, S. K. Datta, O. M. Mukdadi, Dispersion of elastic guided waves in piezoelectric infinite plates with inversion layers, International Journal of Solids and Structures 45 (18) (2008) 5088–5102.

[24] H. Gravenkamp, F. Bause, C. Song, On the computation of dispersion curves for axisymmetric elastic waveguides using the scaled boundary finite element method, Computers and Structures 131 (2014) 46–55.